IEEE Photonics Journal
An IEEE Photonics Society Publication

Open Access

Surface Plasmon Resonance Sensor Based on Microstructured Optical Fiber With Ring-Core Configuration

Volume 8, Number 5, October 2016

Lu Peng
Guiyao Zhou
Mingqin Li
Zhiyun Hou
Changming Xia
Shu Ge

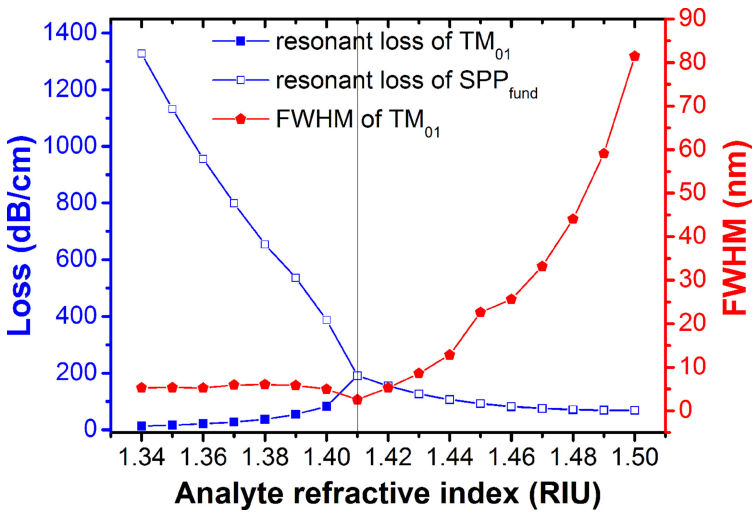

DOI: 10.1109/JPHOT.2016.2613964
1943-0655 © 2016 IEEE

Surface Plasmon Resonance Sensor Based on Microstructured Optical Fiber With Ring-Core Configuration

Lu Peng,[1, 2] **Guiyao Zhou,**[1, 2] **Mingqin Li,**[1, 2] **Zhiyun Hou,**[1, 2] **Changming Xia,**[1, 2] **and Shu Ge**[1, 2]

[1]Guangzhou Key Laboratory for Special Fiber Photonic Devices and Applications, South China Normal University, Guangzhou 510006, China
[2]Guangdong Provincial Engineering Technology Research Center for Microstructured Functional Fibers and Devices, South China Normal University, Guangzhou 510006, China

DOI:10.1109/JPHOT.2016.2613964

Manuscript received August 24, 2016; revised September 20, 2016; accepted September 22, 2016. Date of publication September 29, 2016; date of current version October 19, 2016. This work was supported in part by the National Natural Science Foundation of China under Grant 61377100, Grant 61575066, and Grant 61527822 and in part by Guangdong Natural Science Foundation under Grant 2014A030313428. Corresponding author: G. Zhou (e-mail: gyzhou@scnu.edu.cn).

Abstract: A novel surface plasmon resonance (SPR) sensor based on ring-core microstructured optical fiber with silver film is presented in this paper. Field leakage from the ring core to the central metal film excites plasmon polaritons. Through numerical simulation with the finite-element method, we found that fundamental modes and one of second-order modes have strong interaction with surface plasma modes. Analyzing coupling characteristics, results show that high sensitivity using linear fitting and narrow full-width at half-maximum (FWHM) can both be acquired in these two modes, which contributes to the highest value of figure of merit reaching 2203. The proposed model with two air-hole rings is easy to fabricate in the real operation. Finally, influences of different metal and geometrical parameters on sensing performance are also discussed for optimization further.

Index Terms: Surface plasmon, microstructured optical fibers, fiber optics sensors.

1. Introduction

With the great improvement of science and technology, increasing concerns are being paid to food security, environmental monitoring, and medical treatment. The surface plasma technique has been applied to fiber since it was demonstrated in 1993 by Jorgenson *et al.* [1], which has gained great attention on the sensing field of biology and chemistry for its great potential in monitoring biochemical analyte [2]–[4]. Many types of surface plasmon resonance (SPR) sensors have been reported, including optical Tamm plasmon sensor, plasmonic Fano resonance sensor, and the like [5]–[9]. Although optical Tamm plasmon sensor can achieve sharp resonance and large measurement range, its sensitivity is far lower in terms of the shift of dip wavelength with the increasing of ambient refractive index such as 100 nm/RIU in [5].

The combination of surface plasmon resonance (SPR) and microstructured optical fiber (MOF) provides great possibilities for high sensing performance sensor [10]–[12]. Surface plasmon polaritons are stimulated when photons interact with electrons at the interface between metal and dielectric. A slight change in analyte refractive index (RI) generates a corresponding change in

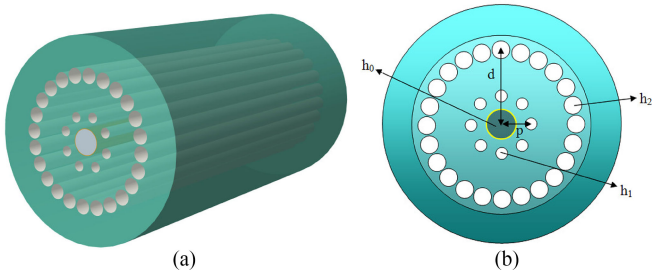

Fig. 1. (a) Three-dimensional schematic and (b) the enlarged cross-section graph of the proposed structure.

the propagation constant of surface plasmon wave, which could also contribute to the variation of coupling condition between the input light and the surface plasma wave [13]. Yu *et al.* designed a selectively metal-coated MOF sensor based on SPR, which can obtain narrow full width at half maximum (FWHM) and higher signal-to-noise ratio [14]. Shuai *et al.* proposed a multi-core MOF model based on the SPR via filling the analyte into the center hole and can achieve high sensitivity and large detection range [15]. Tan *et al.* presented an all-solid D-shaped MOF sensor based on SPR which can realize high sensing performance through phase modulation [16]. However, previous reports concerning SPR sensors mostly consist of hexagonal lattice with circular air-holes, and a few are based on the rectangular lattice [17]–[19].

In this paper, we propose an SPR sensor based on ring-core MOF with silver film pouring into the central air hole wall. Compared with many reported theoretical models with rectangular lattice, this MOF is relatively easier to be fabricated by using general stack-and-draw technology. Leakage from guided light in the large ring-zone will lead to sufficient interaction with internal coating silver film, which provides possibility to achieve high sensing performance, and the proposed sensor could transmit several modes especially TM_{01} mode and HE_{11} modes which could stimulate strong SPR in some conditions, and therefore, we can choose appropriate mode according diverse needs. Through numerical simulation, narrow full width half maximum (FWHM), higher figure of merit (FOM), and large detection range can be achieved, which definitely indicate good performance. Therefore, we suggest that the proposed sensor has great potential to be a candidate in sensing field owing to its feasible structure and excellent performances.

2. Structural Design

As shown in Fig. 1(a), a 3-D structure of the proposed sensor is presented. To present the structure more clearly, we enlarged the cross-section in Fig. 1(b), and it is composed of two layers of air holes with toroidal arrangement surrounding the large center hole. The background material with blue is silica glass. We defined the distance from the centre to the first layer air holes (h1) as the pitch which is equal to 2 μm and used the initial letter "p" to represent the pitch in this paper. The centre of structure is a large air hole (h0) with radius 0.5 p. The first layer air holes' radius h1 and the second layer air holes' radius h2 are equal to 0.2 p, 0.3 p, respectively. According to the theory of total internal reflection, the main guided-wave zone is between the first layer air holes and the second layer air holes where we describe it as ring core. The central air hole wall where we used the yellow to depict is just the position pouring silver into it with thickness of 40 nm and analyte can run in the central hole with gray zone. We use symbol "n_a" to represent analyte RI in the next discussion. The leakage of guided light from the ring-core stimulates the generation of plasmon polaritons and then SPR occurs when its phase meet the matching condition [20], and the distance from the second layer of air holes to the central hole is equal to $d = 2.5$ p. When it comes to specific fabrication of this structure, the central hole consists of a silica tube and then we use eight silica tubes (which constitutes the first layer) to surround the central hole closely. Next, it is supposed to use silica rods to complement the large distance between the first layer and the second layer

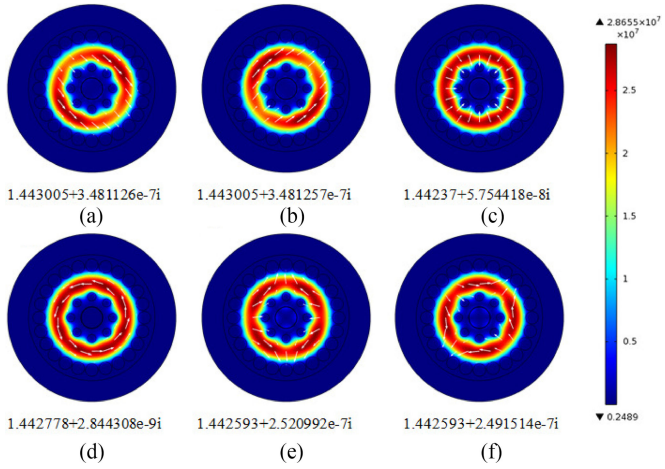

Fig. 2. Distributions of electric fields of fundamental modes and second-order modes at the wavelength 700 nm (a) and (b) are two degenerated fundamental modes with perpendicular orientations each other, which we called HE_{11} modes. (c) Second-order mode that we defined as TM_{01} mode. (d) One of second-order modes; we use TE_{01} to represent this mode. (e) and (f) Two degenerated HE_{21} modes with perpendicular orientations to each other.

before we use twenty-four silica tubes to form the second layer air holes. Every procedure need to prepare carefully to ensure the entire structure is fabricated closely. Finally, this performance can be drawn to MOF by the drawing tower. In terms of the coating, selective coating is more likely to be an appropriate method as in [21]. As for the coupling and receiving of light in the experiment, there is no problem to use traditional experimental method since the central core only occupies a small proportion compared with large ring core, and therefore, it may have few effects on entire coupling and receiving. Specifically, we can use ring source or a spatial light modulator (SLM) to form an annular beam and then couple into ring-core MOF. Receiving light from the proposed fiber can be realized by using general approach because we just need to receive the entire spectrum from the fiber.

In numerical calculation, we use the modified Drude-Lorentz to figure out the dispersion of silver [22]. In addition, the dispersion of silica is also considered by using Sellmeier equation [23]. The outmost layer is the perfect matched layer (PML) which is applied to absorb extra leakage to accurate computation [24].

3. Simulated Results and Analysis

3.1. Mode Analysis

There have been many sensing structures corresponding multiple-core and twin-core based on surface plasmon resonance over the past several years, which were all referred to theory of supermodes because of interaction within core-guided modes when fiber-core is more than one [15], [24], [25]. In this paper, we proposed a ring core structure that consists of two-ring air holes surrounding the large center hole with toroidal arrangement.

Through theoretical simulation, we found that two modes not only fundamental modes but also second-order modes have strong interaction with plasma modes under different analyte RI. As the following Fig. 2, fundamental modes and second-order modes of the proposed structure were presented with respective energetic distributions and electric directions (white arrows). As in Fig. 2(a) and (b), they are two degenerate modes (HE_{11}) with different electric field orientations which are perpendicular to each other. We only consider one of fundamental modes in the next discussion because two degenerate fundamental modes have the same performance in weighing sensing parameters as [25]. As for second-order modes, there are TM_{01}mode (c), TE_{01} mode (d) and two degenerated HE_{21} modes (5), (6) existing in this structure, but we just discuss the TM_{01} mode since

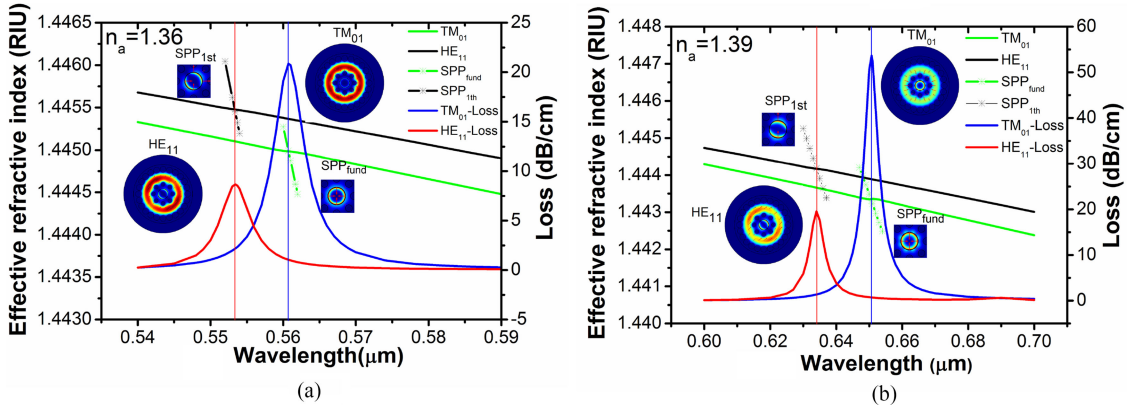

Fig. 3. (a) Dispersive curves and corresponding inserts representing the distribution of electric field under the condition of $n_a = 1.36$. (b) Phase matching relations in the $n_a = 1.39$ with the variation of wavelength.

it can dramatically interact with the plasma wave in certain circumstances. Therefore, we will specifically investigate these two guided-core modes, HE_{11} and TM_{01} mode, for its promising in sensing field. In terms of modes selection, there are several ways to address this problem such as long period fiber Bragg grating (LPFBG) and spatial light modulation (SLM) as in [26]–[28]. Therefore, we consider that this issue can be addressed successfully in the real operation.

3.2 Analysis of Coupling Characteristics

We present dispersive curves and modal attenuation in the following figures in order to investigate the coupling characteristics of the proposed model between ring core modes and plasma modes. Fig. 3(a) shows two prominent confinement loss peaks at the wavelength 553 and 561 nm in the condition of $n_a = 1.36$. Finding the position of loss peak is just the intersection of real part of core mode's effective index and plasmonic mode's effective index, and we use the solid line and the line with symbol to distinguish these different kinds of modes. Combining with inserted graphs which showed electric field distributions of modes, it is easier to demonstrate that TM_{01} mode was resonant with surface plasmonic fundamental mode (SPP_{fund}) while HE_{11} mode was resonant with surface plasmon first-mode (SPP_{1th}). In addition, the intersection of index curves means that the condition of phase matching was satisfied [20]. From that TM_{01} mode's loss is obviously larger than HE_{11} mode's, we can realize that TM_{01} mode's coupling resonance is more strong than HE_{11} mode in this analyte RI. With the increasing of analyte RI, the peak-loss is increasing which means that the coupling resonance is strengthening as shown in Fig. 3(b). It can also demonstrate from the distribution of electric field, the relatively higher analyte RI gives rise to large energy leakage. Taking the increased losses and variation of electric field's distribution into consideration, the presented structure is more sensitive for the higher analyte RI. In addition, the performance of single-peak for each mode indicates that each proposed core-guided mode is only resonant with one plasma mode with the wavelength increases, which is preferable in the application of sensor [15].

To further investigate coupling properties of core modes with variation of analyte RI, several confinement loss figures with electric filed distribution of core are plotted in Fig. 4. The picture on the left shows loss matching condition of TM_{01} mode under analyte RI 1.39, 1.40, 1.41 in Fig. 4(a). As for HE_{11} mode, its confinement loss depends on the wavelength under circumstance of $n_a = 1.41, 1.42, 1.43$ as Fig. 4(b) shown. The solid lines represent core-guided mode's loss and the short dotted curves express plasma modes' loss in Fig. 4(a) and (b). Complete coupling occurs when the core-guided mode's peak-loss is equal to the plasmonic mode's dip-loss according to reference [19]. We can see that two core-guided modes are both closing to the loss matching with analyte RI increases. The TM_{01} mode reaches to loss matching at $n_a = 1.41$ from Fig. 4(a) while HE_{11} mode arrives to its loss matching at $n_a = 1.43$ from Fig. 4(b). Comparing the variation

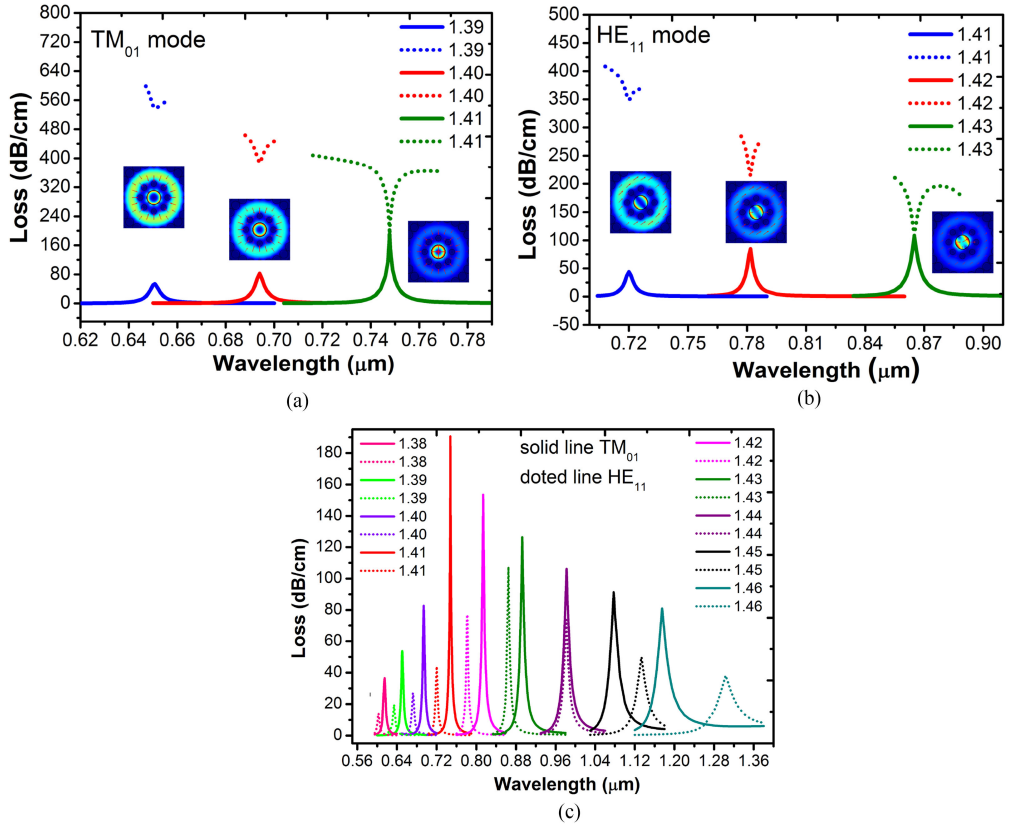

Fig. 4. (a) Loss matching picture of TM_{01} with the $n_a = 1.39$, 1.40, and 1.41, respectively. (b) Loss matching picture of HE_{11} mode with the $n_a = 1.41$, 1.42, and 1.43. (c) Different losses of TM_{01} and HE_{11} from the 1.38 to 1.46 with interval 0.01 depend on wavelength.

of electric field distribution of inserts, it is apparent to observe that distribution of electric filed is weakest when the core-guided mode is at the position of loss matching, which indicates that the leakage of core energy is reaching to the maximum at the complete resonant position. In order to exemplify the position where the confinement loss at the beginning of complete resonance is largest in entire coupling process, we present following figure including losses of TM_{01} mode (solid line) and HE_{11} mode (short dotted line) from the analyte RI 1.38 to 1.46 with the interval of 0.01 in Fig. 4(c). The confinement loss is achieving the largest for TM_{01} in $n_a = 1.41$ and for HE_{11} mode in $n_a = 1.43$, which is consistent with the above-mentioned interpretation about the largest leakage of energy. It is evident from these graphs that TM_{01} mode is faster to reach the complete resonance than HE_{11} mode with the increasing of analyte RI. In addition, the complete resonant loss of TM_{01} mode is higher than the HE_{11} mode's from the figures. Observing the shift of resonant position, we can notice that the presented structure is promising to apply in the refractive sensor.

Next, we show specific coupling properties of these modes at the condition of complete resonance, and phase matching relations are presented in Fig. 5. The TM_{01} mode's index curve has a jump at the wavelength 747 nm, which means an anti-crossing point appears and then the core-guided mode exchanges with the surface plasma fundamental mode towards longer wavelength as the Fig. 5(a) plotted [20]. We can also find that there is difficult to distinguish the TM_{01} mode and plasma fundamental mode from energy fields' distributions, which is coincide with the above analysis corresponding mode's exchange when complete coupling appears between core mode and plasma mode. Combining previous discussions, it displays the electric field energy transforms from core-guided mode to plasmon mode reaching to the largest at the beginning of complete resonance. With the increasing of analyte RI, the anti-crossing point of TM_{01} is more obvious as

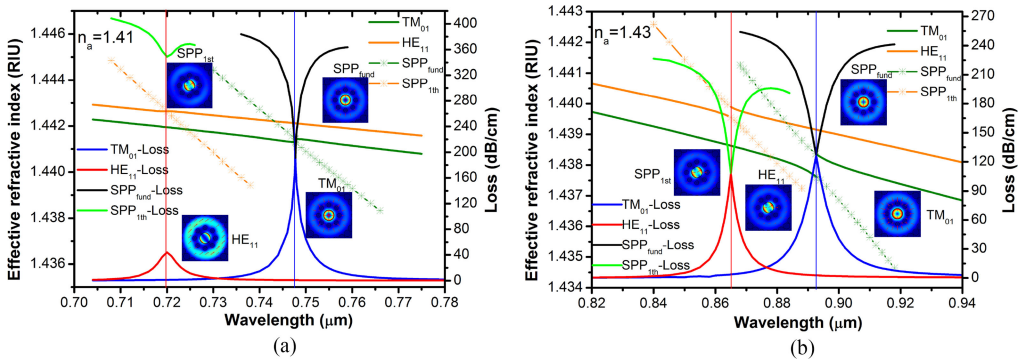

Fig. 5. (a) Complete resonance graph for TM_{01} mode with $n_a = 1.41$. (b) Complete resonance graph for HE_{11} mode with $n_a = 1.43$.

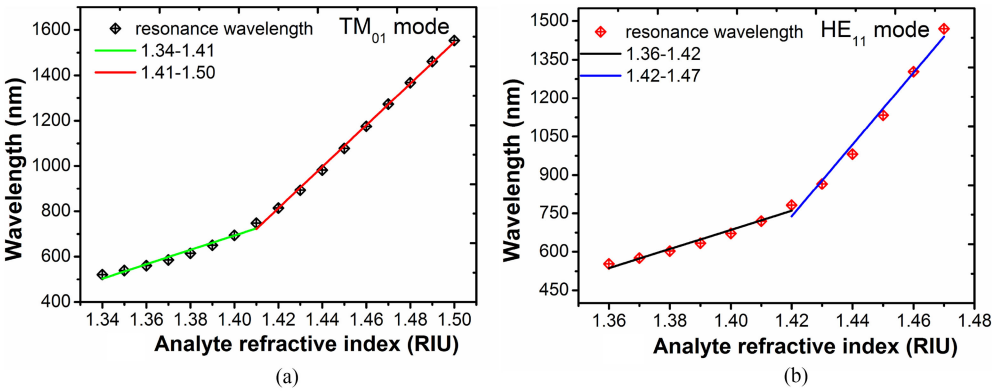

Fig. 6. Fitting graph of TM_{01} mode concerning resonance wavelength with the analyte RI increases. (b) HE_{11} mode's fitting picture of the resonance wavelength as a function of analyte RI.

the Fig. 5(b) depicted. Similarly, the Fig. 5(b) presents the complete resonant characteristics between HE_{11} mode and SPP_{1st} mode. When anti-crossing occurs for HE_{11} mode at the $n_a = 1.43$, two insets of energy distribution about HE_{11} mode and SPP_{1st} mode are almost the same as the Fig. 5(b) plotted.

3.3 Sensing Performance

Through the above discussion, we have a comprehensive understanding for the coupling resonance between core-guided modes and plasma modes. From the shift of resonance wavelength and the change of peak losses under different analytes, we agree that two core-guided modes are both sensitive to the variation of analyte RI. To estimate sensing performance of the proposed structure, sensitivity is an important factor which needs to be considered. According to the formula that the sensitivity is defined as the ratio of resonant wavelength's shift to the change of analyte RI:

$$S = \frac{\partial \lambda_{res}(\text{nm})}{\partial n_a(\text{RIU})}.$$

First, we present two linear fitting graphs in which we choose the method of piecewise fitting, as Fig. 6(a) and (b) show.

For TM_{01} mode, the resonant wavelength's shift was depicted from analyte RI 1.34 to 1.5 with interval 0.01 as shown in Fig. 6(a). The lower index part 1.34–1.41 and the higher part 1.41–1.50 have been fitted, respectively. Fitting results indicate that a slope is 3160.3 in the range of 1.34–1.41 in which resonant wavelengths depend on the analyte RI with linearity 0.96194 while the

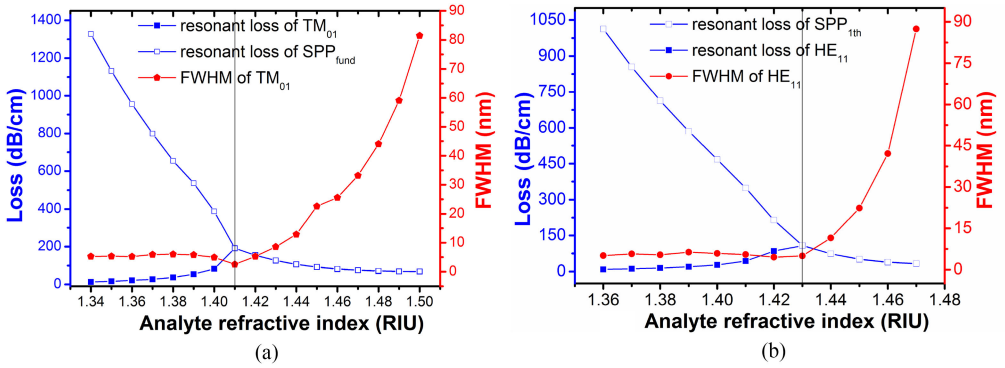

Fig. 7. (a) Solid and hollow blue symbol plot the resonance losses of TM_{01} and SPP_{fund}, respectively. Red symbol depict the FWHM with the increasing of analyte RI. (b) Solid and hollow blue symbol plot the resonance losses of HE_{11} and SPP_{1th}, respectively. Red symbol depicts the FWHM of HE_{11} mode with the increasing of analyte RI.

TABLE 1
Comparison of two modes, including slope, detection range, and linearity

Mode	Slope	Detection range	R-Square
TM_{01}	3160.33	1.34–1.41	0.96194
	9165.25	1.41–1.50	0.99791
HE_{11}	3728.57	1.36–1.42	0.96361
	14016	1.42–1.47	0.98169

slope is 9165.25 in the range of 1.41–1.50 with linearity 0.99791. Fig. 6(b) shows the HE_{11} mode's resonance wavelength with the variation of analyte RI from 1.36–1.47. Though linear fitting, we can obtain that the slope is 3728.57 in the range of 1.36–1.42 with linearity 0.96361, and the slope is 14016 in the range of 1.42–1.47 with linearity 0.98169 which is higher than previous reports [15], [29]. In Table 1, we compare two modes' sensitivity more clearly.

It is well known that the FWHM is also a significant element to weigh accuracy of the detection. Narrow FWHM means excellent sensation to the variation of parameters and guarantees noise's splitting effectively [14]. We calculated two core-guided modes' FWHM as plotted in Fig. 7(a) and (b). Red lines with symbol indicate the FWHM with the change of analyte RI and blue line with symbol depicts core-guided mode's and plasma mode's resonance losses with increasing of the analyte RI. From Fig. 7(a), the narrowest FWHM is 2.58 nm appearing in analyte RI 1.41 due to the beginning of complete resonance, which is much less than previous researches to our best knowledge in this field such as 17 nm in [15] and 13.6 nm in [29]. In addition, the average FWHM can acquire 19.64 nm for TM_{01} mode which is far lower. Similarly, for HE_{11} mode its small FWHM is 4.52 nm occurring in the analyte RI of $n_a = 1.43$ where is also just the beginning of the complete resonance in Fig. 7(b). In the investigation of SPR sensor based on MOF, a narrow FWHM demonstrates good detection accuracy and good reliability.

Now, we use another more comprehensive parameter, i.e., figure of merit (FOM), to explore our proposed structure. According to the equation

$$\mathrm{FOM} = m(\mathrm{ev.RIU}^{-1})/\mathrm{FWHM(ev)}$$

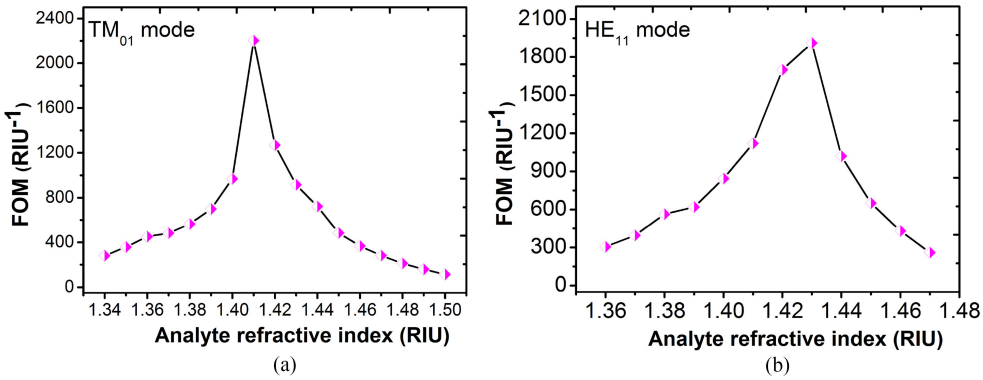

Fig. 8. (a) FOM of TM_{01} mode with the variation of analyte RI. (b) FOM for HE_{11} mode with the analyte RI increases.

where m is the slope of the resonance peak position per RIU. It is clear from the above formula to know that FOM is taking the sensitivity and FWHM both into consideration which demonstrates the sensing performance better [14], [15], [30]. We calculated two modes' value of FOM as Fig. 8 plotted. For TM_{01} mode, FOM is maintaining a dramatically rise with the increasing of analyte RI in the range of 1.34–1.41. The largest value 2203 of FOM occurs in the $n_a = 1.41$ and then decreases with the increasing of analyte RI from 1.41–1.50. As for the HE_{11} mode, the largest FOM is 1911 which appears at $n_a = 1.43$ and then declines with the analyte RI increases. Considering previous analysis, there is no doubt that the largest value of FOM is caused by the beginning of complete resonance. Furthermore, the obtained largest value of FOM 2203 is far more exceeding previous reports.

These results indicate that TM_{01} mode has large detection range, excellent FOM and the fitting result of sensitivity has better linearity for higher analyte RI comparing with HE_{11} mode. Besides, HE_{11} mode has highest sensitivity which is higher than the TM_{01} mode from 1.42–1.47. Considering above factors, we suggest that two core-guided modes have their own advantages. For preparatory detection, it's better to choose the TM_{01} mode for its' large detection range. In addition, for high analyte RI, it is also a good choice to select the HE_{11} mode for its high sensitivity.

4. Discussion

4.1 Comparing the Influence of Ag and Au on the Sensing Performance

Generally speaking, gold and silver are the most common metal in the investigation of surface plasmon resonance. In this paper, we used silver in the proposed structure and acquired high sensitivity and excellent FOM. Next we will study the influence of gold on the sensing performance. Through numerical simulation, we fitted TM_{01} mode's resonant wavelength with the range of analyte RI 1.38–1.5. For refractive index lower than 1.38, gaining far small loss is not beneficial to accurate sensing detection, and for RI higher than 1.5, resonance wavelength is exceeding 1800 nm which is not appropriate for the investigation [32]. Therefore, we display the range of analyte RI from 1.38 to 1.50 for gold-filling. Apparently, the slope is 3611 in the range of 1.38–1.41 with linearity 0.9865 and then the slope is 8743.8 in the range of 1.41–1.5 with the linearity 0.99588. Next, we consider the FWHM and resonant loss to weigh the sensing performance better in Fig. 9(b). As shown, red line presents the value of FWHM which depends on analyte RI, and blue line indicates resonant loss under the different analyte. Clearly, largest resonant loss is over 250 dB/cm and narrowest FWHM is 5 nm.

With these results corresponding gold, we make a comparison with previous discussion of silver. Relatively large loss can realize via filling gold, but lower loss is more favorable for real application due to sensing length [33]. In addition, narrowest FWHM and higher sensitivity can be achieved via filling silver. Furthermore, the detection range when filling with Ag is from 1.34 to 1.50 which is

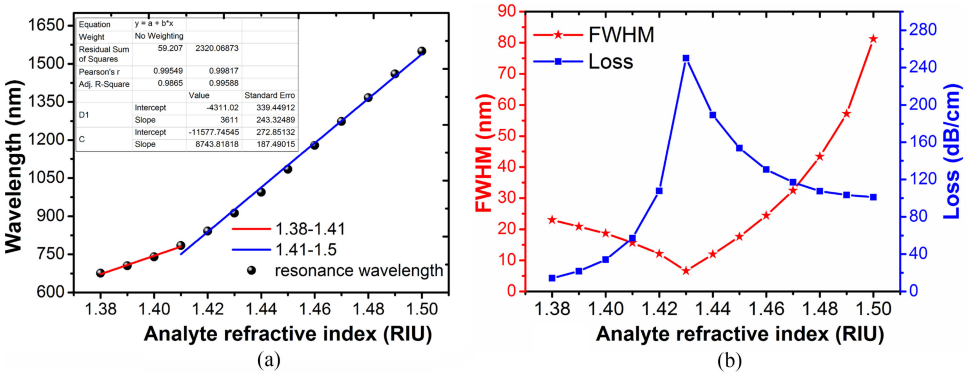

Fig. 9. (a) Fitting graph about resonance wavelength dependence on analyte RI of model by replacing the metal with gold. (b) Blue curve represents the resonance loss and red symbols indicate FWHM with the change of analyte RI.

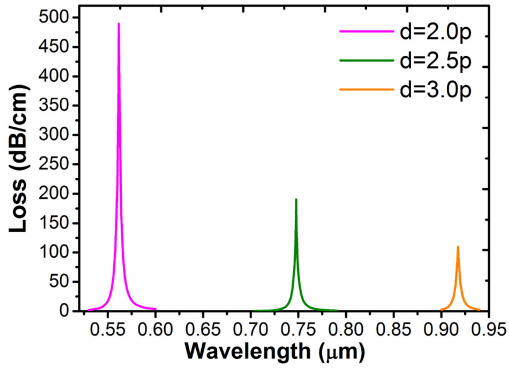

Fig. 10. Confinement losses when the model with different d is reaching toward the complete resonance under different analyte RI. Magenta line plots d = 2.0 p with $n_a = 1.35$, the green curve indicates d = 2.5 p with $n_a = 1.41$, and the orange curve depicts d = 3.0 p with $n_a = 1.44$.

broader than pouring the Au from 1.38 to 1.50. Thus, we believe that the proposed structure has better sensing performance with silver film.

4.2 The Variation of Parameters to Optimize Sensing Performance

The above discussions are based on uniform parameters of p = 2 μm, h0 = 0.5 p, h1 = 0.2 p, h2 = 0.3 p, d = 2.5 p, ansth = 40 nm. There is no doubt that the value of d has an effect on sensing performance. We will discuss specific impacts of this distance from the second layer air holes to the centre hole on the coupling resonance. From the Fig. 10, three loss curves are displayed with different values of d. The following three curves are all reaching to beginning of complete resonances in which different colors represent different values of d under different analyte RI. For the magenta line which depicts at the $n_a = 1.35$ with d = 2.0 p. And the olive line plots the condition of $n_a = 1.41$ with d = 2.5 p, which is consistent with our previous presented structure. As for the orange line displays the condition of $n_a = 1.44$ and d = 3.0 p. Looking at the value of loss, the largest loss of magenta line is significantly higher than others, which indicates the coupling resonance is stronger because the waveguide region is more closing to the coating film under this circumstance. With the increasing of d, the confinement loss reduces obviously owing to increasing distance between ring-core and coating film and thinning energy density. We can see that the largest loss is around 100 dB/cm at d = 3.0 p, but it also means small measurement range because the peak-loss may reduce quickly with the variation of analyte RI.

Although the largest loss of the proposed model with d = 2.5 p is around 190 dB/cm, it has some improvements compared with many previous reports such as highest losses exceeding 1000 dB/cm in [10], about 570 dB/cm in [32], and approaching 370 dB/cm in [15]. Actually, relatively large loss is also related with large resonance depth and the loss in our structure decreases quickly with the slight increasing of wavelength, which indicates high signal-to-noise ratio as in [14]. Large loss always means small sensor length which is not favorable in the real operation, but the millimeter scale length had already been investigated in [33]. Therefore, we consider that our sensor with several millimeter lengths can be realized through effective experimental scheme and precise equipments as provided in [15].

5. Conclusion

We presented a sensor model based on a ring core MOF in this paper. A series of phase matching relations are performed from incomplete resonance to complete resonance. Two modes, i.e., the HE_{11} mode and the TM_{01} mode, can both achieve excellent sensing performance through our accurate calculation. Especially, the lowest FWHM that be achieved is 2.58 nm, which leads to highest value of FOM, and a large detection range from 1.34 to 1.50 can be acquired as well. A comparison with gold demonstrates that our model with silver can attain a better sensing performance. Finally, we discussed the influence of different values of d on the model performance in order to optimize structure further.

References

[1] R. Jorgenson and S. Yee, "A fiber-optic chemical sensor based on surface plasmon resonance," *Sens. Actuators B, Chem.*, vol. 12, pp. 213–220, 1993.

[2] A. Dhawan, M. D. Gerhold, and J. F. Muth, "Plasmonic structures based on subwavelength apertures for chemical and biological sensing applications," *IEEE Sensors J.*, vol. 8, no. 6, pp. 942–950, Jun. 2008.

[3] N. Livnat Levanon, E. Vigonsky, and O. Lewinson, "Real time measurements of membrane protein:receptor interactions using surface plasmon resonance (SPR)," *J. Vis. Exp.*, vol. 93, 2014, Art. no. e51937, doi: 10.3791/51937.

[4] J. Zhou *et al.*, "Intensity modulated refractive index sensor based on optical fiber Michelson interferometer," *Sens. Actuators B, Chem.*, vol. 208, pp. 315–319, Nov. 2014.

[5] C. Jocher *et al.*, "Fiber based polarization filter for radially and azimuthally polarized light," *Opt. Exp.,* vol. 19, no. 20, pp. 19582–19590, 2011.

[6] M. A. Schmidt, D. Y. Lei, L. Wondraczek, V. Nazabal, and S. A. Maier, "Hybrid nanopartical-microcavity-based plasmonic nanosensors with improved detection resolution and extended remote-sensing ability," *Nature Commun.*, vol. 3, 2012, Art. no. 1038, doi: 10.1038/ncomms2109.

[7] D. Y. Lei, J. T. K. Wan, and H. C. Ong, "Numerical and analytical evaluations of the sensing sensitivity of waveguide mode in one-dimensional metallic gratings," *Nanotechnol.*, vol. 23, 2012, Art. no. 275501, doi: 10.1088/0957-4484/23/27/275501.

[8] Z. H. Yong, D. Y. Lei, C. H. Lam, and Y. Wang, "Ultrahigh refractive index sensing performance of plasmonic quadrupole resonances in gold nanoparticles," *Nanoscale Res. Lett*, vol. 9, no. 1, pp. 1–6, 2014, doi: 10.1186/1556-276X-9-187.

[9] M. Konig *et al.*, "Unveiling the correlation between nanometer-thick molecular monolayer sensitivity and near-field enhancement and localization in coupled plasmonic oligomers," *ACS Nano*, vol. 8, no. 9, pp. 9188–9198, 2014, doi: 10.1021/nn5028714.

[10] R. Otupiri, E. K. Ahowuah, S. Haxha, H. Ademgil, F. AbdelMalek, and A. Aggoun, "A novel birefrigent photonic crystal fiber surface plasmon resonance biosensor," *IEEE Photon. J.*, vol. 6, no. 4, Aug. 2014, Art. no. 6801711, doi: 10.1109/JPHOT.2014.2335716.

[11] X. H. Zhao *et al.*, "Improvement of the sensitivity of the surface plasmon resonance sensors based on multi-layer modulation techniques," *Opt. Commun.*, vol. 335, pp. 32–36, Jan. 2015, doi: 10.1016/j.optcom.2014.09001.

[12] M. Tian, P. Lu, L. Chen, L. V. Chao, and D. M. Liu, "All-solid D-shaped photonic fiber sensor based on surface plasmon resonance," *Opt. Commun.*, vol. 285, pp. 1550–1554, 2012.

[13] J. Homola, *Surface Plasmon Resonance Based Sensors*. Berlin, Germany: Springer-Verlag, 2006.

[14] X. Yu *et al.*, "A selectively coated photonic crystal fiber based surface plasmon resonance sensor," *J. Opt.*, vol. 12, Jan. 2010, Art. no. 015005, doi: 10.1088/2040-8978/12/1/015005.

[15] B. B. Shuai, L. Xia, Y. T. Zhang, and D. M. Liu, "A multi-core holey fiber based plasmonic sensor with large detection range and high linearity," *Opt. Exp.*, vol. 20, pp. 5974–5986, Mar. 2012, doi:10.1364/OE.20.005974.

[16] Z. X. Tan, X. Hao, Y. H. Shao, Y. Z. Chen, X. J. Li, and P. Fan, "Phase modulation and structural effects in a D-shaped all-solid photonic crystal fiber surface plasmon resonance sensor," *Opt. Exp.*, vol. 22, pp. 15049–15063, Jun. 2014, doi:10.1364/OE.22.015049.

[17] F. K. Shi, L. Peng, G. Y. Zhou, X. L. Cang, Z. Y. Hou, and C. M. Xia, "An elliptical core D-shaped photonic crystal fiber-based plasmonic sensor at upper detection limit," *Plasmonics*, vol. 10, pp. 1263–1268, 2015, doi: 10.1007/s11468-9931-4.
[18] Z. K. Fan *et al*., "High sensitivity of refractive index sensor based on analyte-filled photonic crystal fiber with surface Plasmon resonance," *IEEE Photon. J.*, vol. 7, no. 3, Jun. 2015, Art. no. 4800809, doi: 10.119/JPHOT.2015.2432079.
[19] G. W. An, S. G. Li, W. Qin, W. Zhang, Z. K. Fan, and Y. J. Bao, "High-sensitivity refractive index sensor based on D-shaped photonic crystal fiber with rectangular lattice and nanoscale gold film," *Plasmonics*, vol. 9, pp. 1355–1360, 2014, doi: 10.1007/s11468-014-9749-5.
[20] Z. H. Zhang, Y. F. Shi, B. M. Bian, and J. Lu., "Dependence of leaky mode coupling on loss in photonic crystal fiber with hybrid cladding," *Opt. Exp.*, vol. 16, no. 3, pp. 1915–1922, Feb. 2008.
[21] X. Zhang, R. Wang, F. M. Cox, B. T. Kuhlmey, and M. C. J. Large, "Selective coating of holes in microstructured optical fiber and its application to in-fiber absortive polarizers," *Opt. Exp.*, vol. 15, no. 24, pp. 16270–16278, Nov. 2007.
[22] D. Rioux, S. Vallieres, S. Besner, E. Mazur, and M. Meunier, "An analytic model for the dielectric function of Au, Ag, and their alloys," *Adv. Opt. Mater.*, vol. 2, pp. 176–182, Feb. 2014, doi:10.1002/adom.201300457.
[23] W. Sellmeier, "Zur erklarung derabnormen farbenfolge im spectrum einiger substanzen," *Ann. Phys. Chem.*, vol. 219, no. 6, pp. 272–282, 1871, doi: 10.1002/andp.18712190612.
[24] S. Y. Zhang *et al*., "Theoretical study of dual-core photonic crystal fibers with metal wire," *IEEE Photon. J.*, vol. 4, no. 4, pp. 1178–1187, Aug. 2012.
[25] W. E. P. Padden, M. A. van Eijkelenborg, A. Argyros, and N. A. Lssa, "Coupling in a twin-core microstructured polymer optical fiber," *Appl. Phys. Lett.*, vol. 84, pp. 1689–1691, 2004, doi:10.1063/1.1651651.
[26] W. V. Sorin, B. Y. Kim, and H. J. Shaw, "Highly selective evanescent modal filter for two-mode optical fibers," *Opt. Lett.*, vol. 11, no. 9, pp. 581–583, 1986, doi: 10.1364/OL.11.000581.
[27] C. Jocher *et al*., "Fiber based polarization filter for radially and azimuthally polarized light," *Opt. Exp.*, vol. 19, no. 20, pp. 19582–19590, 2011.
[28] I. Moreno, J. A. Davis, I. Ruiz, and D. M. Cottrell, "Decomposition of radially and azimuthally polarized beams using a circular-polarization and vortex-sensing diffraction grating," *Opt. Exp.*, vol. 18, no. 7, pp. 7173–7183, 2010.
[29] L, Peng, F. K. Shi, G. Y. Zhou, S. Ge, Z. Y. Hou, and C. M. Xia, "A surface plasmon biosensor based on D-shaped microstructured optical fiber with rectangular lattice," *IEEE Photon. J.*, vol. 7, no. 5, Oct. 2015, Art. no. 4801309.
[30] L. J. Sherry, S. H. Chang, G. C. Schatz, and D. R. P. Van, "Localized surface plasmon resonance spectroscopy of single silver nanocubes," *Nano Lett.*, vol. 5, pp. 2034–2038, 2005, doi: 10.1021/nl0515753.
[31] W. Jin, Z. Zhang, and J. Ju, "Two-mode photonic crystal fibers," *Opt. Exp.*, vol. 13, pp. 2082–2088, Mar. 2005.
[32] G. W. An, S. G. Li, W. Qin, W. Zhang, Z. K. Fan, and Y. J. Bao, "High-sensitivity refractive index sensor based on D-shaped photonic crystal fiber with rectangular lattice and nanoscale gold film," *Plasmonics*, vol. 9, pp. 1355–1360, 2014, doi: 10.1007/s11468-014-9749-5.
[33] H. W. Lee, M. A. Schmidt, H. K. Tyagi, L. P. Sempere, and P. St. J. Russell, "Polarization-dependent coupling to plasmon modes on submicron gold wire in photonic crystal fiber," *Appl. Phys. Lett.*, vol. 93, no. 11, 2008, Art. no. 111102.